Chinese Chemical Letters 36 (2025) 109885

Contents lists available at ScienceDirect

Chinese Chemical Letters

journal homepage: www.elsevier.com/locate/cclet

In situ regeneration of catalyst for Fenton-like degradation by photogenerated electron transportation: Characterization, performance and mechanism comparison

Ming-Zhen Li[a], Yang Zhang[a,b,*], Kun Li[a], Ya-Nan Shang[a,c], Yi-Zhen Zhang[a], Yu-Jiao Kan[a], Zhi-Yang Jiao[a], Yu-Yuan Han[a], Xiao-Qiang Cao[a,d,*]

[a] College of Safety and Environmental Engineering, Shandong University of Science and Technology, Qingdao 266590, China
[b] Engineering Research Center of Groundwater Pollution Control and Remediation, Ministry of Education of China, Beijing Normal University, Beijing 100875, China
[c] Environment Research Institute, Shandong University, Qingdao 266237, China
[d] Institute of Yellow River Delta Earth Surface Processes and Ecological Integrity, Shandong University of Science and Technology, Qingdao 266590, China

ARTICLE INFO

Article history:
Received 23 December 2023
Revised 31 March 2024
Accepted 11 April 2024
Available online 13 April 2024

Keywords:
Electron transportation
Catalyst regeneration
Peroxymonosulfate
Co
Photocatalytic

ABSTRACT

Inactivation of carbon-based transition metal catalysts, which was caused by electron loss, limited their application in advanced oxidation processes. Therefore, Co and TiO_2 double-loaded carbon nanofiber material (Co@CNFs-TiO_2) was synthesized in this study. Photocatalytic and chemical catalytic systems were synergized efficiently. Tetracycline was eliminated within 15 min. The degradation rate remained above 90% after five cycles, and the 50% promotion proved the high stability of Co@CNFs-TiO_2. The main reactive oxygen species in this system were sulfate radicals, whereas Co and TiO_2 represented the active sites of the catalytic reaction. Electrons generated from TiO_2 during the photocatalytic process were transferred to Co, which promoted the Co(III)/Co(II) cycle and maintained Co in a low-valence state, thereby stimulating the generation of sulfate radicals. In this study, the effective regulation of reactive oxygen species in the reaction system was realized. The results provided a guidance for *in situ* electron replenishment and regeneration of carbon-based transition metal catalysts, which will expand the practical application of advanced oxidation processes.

The degradation of antibiotic contamination was an urgent problem to be solved in the field of water treatment [1]. Tetracycline (TC), a widely used antibiotic, poses several potential threats to the environment and human health [2,3]. Due to the wide pH range and high free radical potential [4], peroxymonosulfate (PMS) based advanced oxidation processes (AOPs) had practical applications in antibiotic pollution treatment [5]. Furthermore, carbon-based transition metal catalysts could efficiently activate PMS to produce multiple reactive oxygen species (ROS) for pollutant degradation and reduce agglomeration and secondary pollution [6]. Among various ROS generated in this system, sulfate radicals had a higher redox potential (3.1 eV) and exhibited a better degradation efficiency with respect to complex organic compounds [7,8]. However, as the valence states of the transition metals increase, the production of sulfate radicals decreases [9]. Therefore, electron supply was necessary to reduce transition metals, ensuring the continuous and stable generation of sulfate radicals [10]. The key to addressing this issue lies in identifying effective *in situ* electron sources [11].

As a classic catalytic reaction system, photocatalysis was a typical electron-supply reaction process. At the core of photocatalysis, catalysts (such as TiO_2) could produce electrons (e^-) and holes (h^+) under the action of light [12]. Holes were highly oxidized and could react with water molecules or hydroxyl radicals to generate hydroxyl radicals for the degradation of the target pollutant. Due to the electrostatic forces, e^- and h^+ were easily compounded during the transmission process [13]. Therefore, one of the keys to improve photocatalytic efficiency was to accelerate electron transmission and provide electron receptors to avoid the formation of a composite. To solve this problem, researchers had adopted material doping [14].

Previous studies showed that the photocatalytic system was limited to electron transfer and e^-/h^+ separation efficiency.

* Corresponding authors at: College of Safety and Environmental Engineering, Shandong University of Science and Technology, Qingdao 266590, China.
E-mail addresses: Zhangyang@sdust.edu.cn (Y. Zhang), caoxiaoqiang@sdust.edu.cn (X.-Q. Cao).

https://doi.org/10.1016/j.cclet.2024.109885
1001-8417/

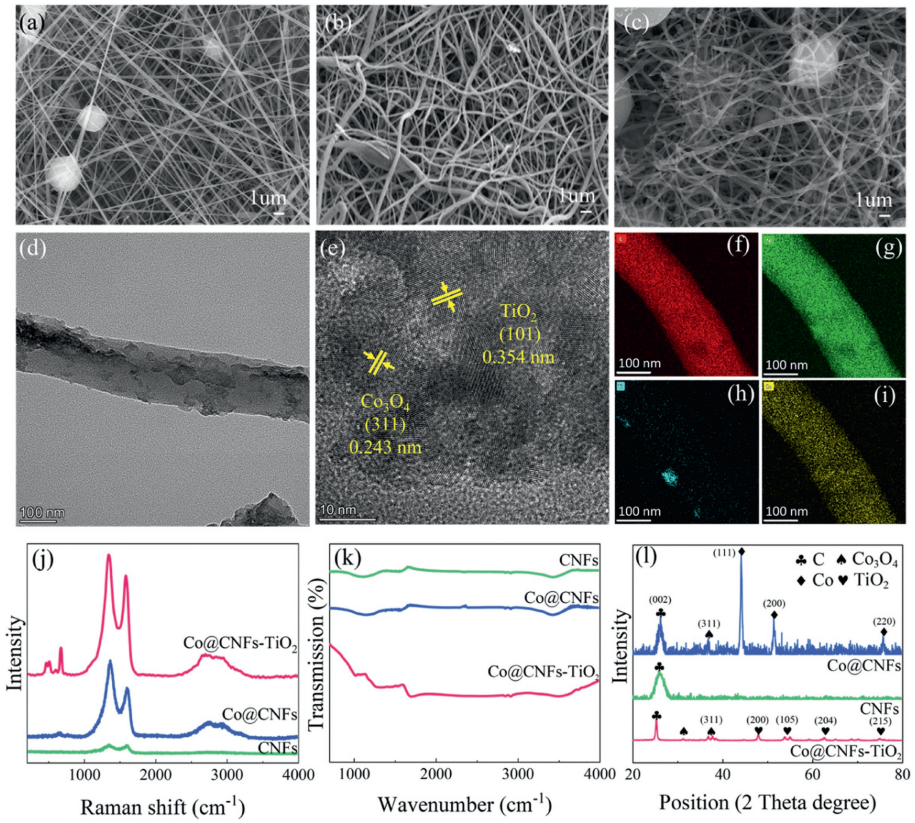

Fig. 1. SEM image of CNFs (a), Co@CNFs (b) and Co@CNFs-TiO_2 (c). TEM (d) and HRTEM (e) patterns of Co@CNFs-TiO_2. EDS elemental mapping of Co@CNFs-TiO_2 (f-i), Raman spectra (j), FTIR spectra (k) and XRD patterns (l) of different samples.

Carbon-supporting transition metal catalysts had problems with increasing metal valence and catalyst aging [15]. A carbon-supported transition metal catalysis/photocatalyst synergistic system, that is, a combination of the two systems, could be used to overcome the disadvantages of a single catalytic system [16]. The photocatalytic process generates e^- and h^+, which could be used as a supplementary source of electrons to accelerate the valence cycle of transition metals; thus, they were in a low-valence state for efficient catalysis, and catalyst regeneration and continuous activation could be realized. As a shallow potential trap for photogenerated electrons, metal atoms could prolong the recombination time of e^-/h^+, accelerate electron transport, facilitate the degradation of pollutants by h^+, and improve photocatalytic efficiency [17].

As typical one-dimensional materials, carbon nanofibers (CNFs) could be used as catalyst carrier to verify this finding because of their high specific surface area, large aspect ratio, high thermal and chemical stability. Further, electrospinning was known to be a simple and inexpensive way to generate nanofiber supported catalysts. Thus cobalt-doped carbon nanofiber-supported TiO_2 (Co@CNFs-TiO_2) catalysts were prepared via electrospinning, carbonization, and the sol-gel method (Appendix S1 in Supporting information). The catalysts were subsequently characterized using multiple methods (Appendix S2 in Supporting information). The synergistic catalytic performance and *in situ* regeneration effect of the catalyst were evaluated using TC degradation (Appendix S3 in Supporting information). The reaction characteristics and catalytic mechanism of the synergistic system were revealed. In this study, a new concept was introduced based on which the long-term stability of AOPs could be achieved, which will effectively extend its applications.

As depicted in Figs. 1a–c, CNFs, Co@CNFs and Co@CNFs-TiO_2 exhibited the characteristic nanofiber structure in scanning electron microscope (SEM) analyses. After carbonization, Co@CNFs and Co@CNFs-TiO_2 showed a spatially interconnected structure, contributing to increased material stability and providing ample space for reactions [18]. TEM studies revealed a uniform distribution of titanium dioxide on the surface of carbon nanofibers (Fig. 1d). The structure of the catalysts was determined using HRTEM images of Co@CNFs-TiO_2. As shown in Fig. 1e, the lattice structure and crystal morphology showed that the lattice spacings were 0.354 and 0.243 nm, respectively, corresponding to the spacings between the TiO_2 (101) and Co_3O_4 (311) planes. The distributions of C, N, Ti, and Co were showed in Figs. 1f–i. As shown in Fig. 1g, the uniform distribution of N inside the CNFs accelerates electron transfer during the reaction. The energy dispersive X-ray spectroscopy (EDX) spectra confirmed the distribution of these elements with concentrations of 0.81% and 3.55%, respectively (Fig. S1 in Supporting information).

Fig. 1j showed the Raman spectra of the materials. Significant G and D bands were observed in the spectra of CNFs, Co@CNFs, and Co@CNFs-TiO_2. The I_G/I_D values of them were 0.92, 0.70, and 0.83, respectively, which means that the amorphous carbon content in all materials was higher than the crystalline carbon concentration. Co@CNFs-TiO_2 exhibits vibration peaks at 141 cm^{-1} (E_g), 396 cm^{-1} (B_{1g}), 515 cm^{-1} (A_{1g}), and 640 cm^{-1} (E_g), which correspond to the Raman activation mode of anatase. These results indicated that the TiO_2 in catalysts was an anatase crystal. Functional groups of the catalysts were identified based on their FTIR spectra (Fig. 1k). Note that all spectra had small peaks in the range of 3200–3700 cm^{-1} and at 1600 cm^{-1} corresponding to the stretching vibration of O–H and the bending vibration of C≡C, respectively. The characteristic peak of Co@CNFs-TiO_2 at 450–600 cm^{-1} corresponded to the tensile vibration of Ti-O-Ti, confirming the formation of TiO_2. X-ray diffraction (XRD) patterns of the materials were shown in

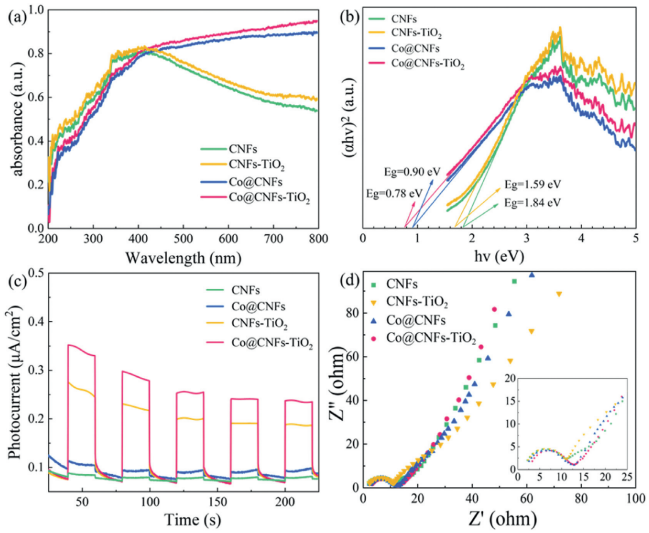

Fig. 2. UV–vis spectra of CNFs, CNFs-TiO_2, Co@CNFs and Co@CNFs-TiO_2 (a), and the plot of transformed Kubelka-Munk function *versus* the energy of light (b). (c) Transient photo-current response of Co@CNFs, CNFs-TiO_2, Co@CNFs and Co@CNFs-TiO_2. (d) Electrochemical impedance spectroscopy of CNFs, CNFs-TiO_2, Co@CNFs and Co@CNFs-TiO_2.

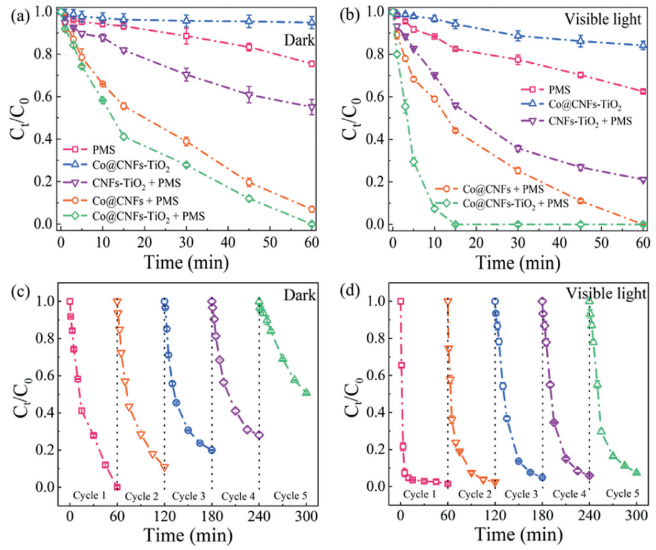

Fig. 3. Degradation of multiple materials in dark (a) and light (b) systems. Cyclic degradation in dark (c) and light (d) systems. TC, 67 μmol/L; PMS, 1 mmol/L; catalyst, 0.2 g/L.

Fig. 1l. The diffraction peaks of Co@CNFs and Co@CNFs-TiO_2 at 2θ were 44.2°, 51.5°, and 75.9°, corresponding to Co (JCPDS No. 89–7093). Notably, a peak at 36.8° was observed, corresponding to the Co_3O_4. However, no notable Co (JCPDS No. 89-7093) was detected in Co@CNFs-TiO_2. Therefore, it was speculated that Co was oxidized during secondary heating. Based on the 2θ reflections of 25.354° (101), 37.895° (004), 48.13° (200), 54.08° (105), 62.8° (204), and 75.26° (215) in the XRD pattern, TiO_2 was confirmed to be an anatase phase.

To understand the bonding behavior between the atoms in Co@CNFs-TiO_2, the X-ray photoelectron spectroscopy (XPS) spectra of Co, C, O, and Ti were analyzed. The Co 2p spectrum of Co@CNFs-TiO_2 (Fig. S2a in Supporting information) showed peaks at 780.5 and 795.8 eV, corresponding to Co $2p_{3/2}$ and Co $2p_{1/2}$ states, whereas the two oscillating satellite centers were located at 785.7 and 803.4 eV, respectively. These were characteristics of Co_3O_4. The C 1s spectrum (Fig. S2b in Supporting information) showed peaks at 284.4, 285.6, and 288.3 eV, corresponding to sp^2-C (C=C), sp^3-C, and C=O, respectively. Fig. S2c (Supporting information) revealed that the two main peaks of O 1s were located at 529.6 and 531.5 eV, respectively, corresponding to lattice oxygen in Co oxide and surface oxygen in TiO_2. The Ti 2p spectrum had two peaks at 458.4 and 464.1 eV (Fig. S2d in Supporting information), which correspond to the binding energy of Ti $2p_{1/2}$ and Ti $2p_{3/2}$, respectively. The combination with the O 1s spectrum showed that a certain amount of TiO_2 was supported on the surface of Co@CNFs-TiO_2.

The photochemical properties of the different supported catalysts were compared. Fig. 2a showed the UV–vis absorption spectrum of the sample. Compared with CNFs, the light absorption boundary of the materials after Co and TiO_2 loading showed a redshift, which could improve the utilization rate of the sample with respect to light. It was beneficial for improving the photocatalytic efficiency. The band gaps of CNFs, Co@CNFs, CNFs-TiO_2 and Co@CNFs-TiO_2 catalytic materials were 1.84, 0.90, 1.59 and 0.78 eV, respectively (Fig. 2b). The photocurrent responses of CNFs, Co@CNFs, CNFs-TiO_2, and Co@CNFs-TiO_2 were obtained in light irradiation for five on-off cycles (Fig. 2c). Co@CNFs-TiO_2 exhibited a higher photocurrent intensity, indicating faster photoexcited e^- transfer and less recombination of e^-/h^+. The electrochemical impedance spectroscopy (EIS) Nyquist plots in the dark were showed in Fig. 2d. Co-doping increased the electron transfer and the separation efficiency of photogenerated electron-holes increased after the TiO_2 loading, which reduced the resistance of the material. The results showed that Co@CNFs-TiO_2 exhibits an optimal photocurrent response and that e^- could be generated and transferred efficiently, which enhances the catalytic activity.

TC was used as the target pollutant and the catalytic performance in different reaction systems. Figs. 3a and b showed that Co@CNFs-TiO_2 exhibits a negligible performance, achieving a 5.1% removal of TC from the aqueous solution in 60 min, indicating that the surface adsorption was poor. However, it could be speculated that the 16% decrease of TC concentration in light was due to the formation of photogenerated electrons and holes in the system. PMS could degrade TC in both dark and light environments. Because UV light could activate PMS, light irradiation increased the degradation rate of TC by 13%. For the same reason, Co@CNFs achieve a 6% higher degradation efficiency in the light system than in the dark environment and the doping of Co improves the degradation of pollutants to 98% in 60 min [9]. The degradation curve of Co@CNFs-TiO_2-activated PMS in a dark environment showed a similar trend to that of Co@CNFs. The small difference might be attributed to the exposure of more Co active sites during secondary heating. The degradation rate reached 100% in 15 min for the Co@CNFs-TiO_2 activation of the PMS system under light conditions, which was 56% higher than that of Co@CNFs. Further, the reaction rate constant exhibited consistent regularity with degradation (Table S1 in Supporting information). The intermediates could be fully mineralized in 120 min (Fig. S3 in Supporting information). Co and TiO_2 had an electron transfer effect that promotes the activation of PMS, thus improving the degradation rate and efficiency of pollutants. In addition, there was a positive correlation between the degradation rate and light intensity, indicating the significant enhancing effect on the reaction process (Fig. S4 in Supporting information).

The stability of the catalyst was verified *via* five cycles of Co@CNFs-TiO_2 activation PMS system under light conditions. Figs. 3c and d showed that the degradation effect of the catalyst was slightly weakened after five degradation cycles, but the efficiency of the fifth degradation reached 90%, which proved that Co@CNFs-TiO_2 had a good stability. However, Co@CNFs-TiO_2 could

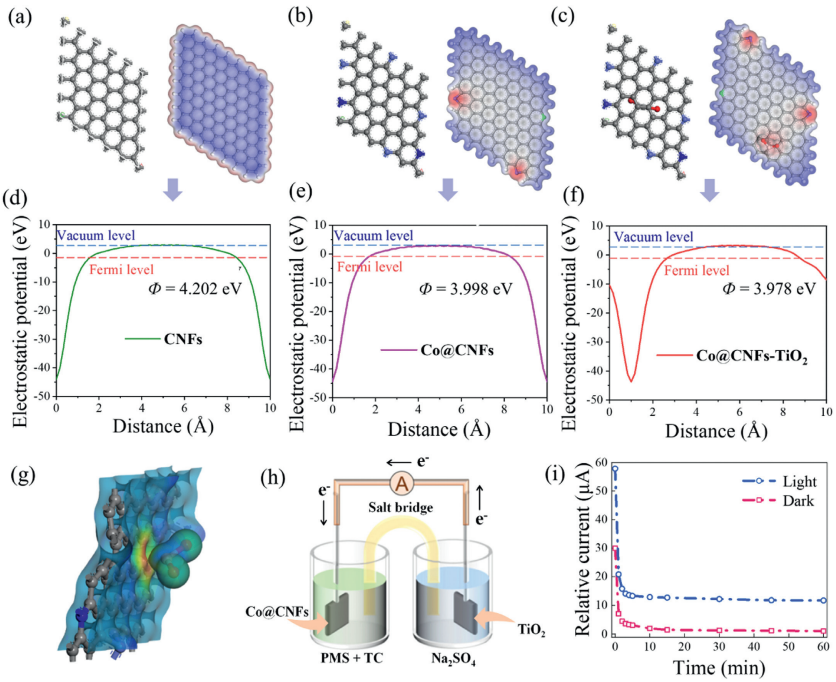

Fig. 4. Optimized structure models and calculated electrostatic potentials of CNFs (a), Co@CNFs (b), and Co@CNFs-TiO_2 (c). The working functions of CNFs (d), Co@CNFs (e), and Co@CNFs-TiO_2 (f). (g) Differential charge density image of Co@CNFs-TiO_2. The built GOS system (h) and current flowing (i) from PMS/pollutant cell to the Na_2SO_4.

only maintain 40% efficiency after five cycles in the dark, indicating that electron transportation effectively promoted the *in situ* regeneration of the catalyst, leading to a sustained and stable catalytic effect.

To understand the degradation mechanism, quenching experiments were performed to determine the ROS levels in the solution (Figs. S5a and b in Supporting information). The addition of certain concentrations of *tert*–butanol (TBA) and *p*-benzoquinone (*p*-BQ) inhibited the degradation of TC and the degradation rates decreased to 97.6% and 93.9%, respectively, indicating that the reaction system contained small amounts of $^{\bullet}OH$ and $^{\bullet}O_2^-$ and the effect was relatively weak. After the addition of ammonium oxalate (AO), methanol (MeOH), and $AgNO_3$, the TC degradation rates decreased to 72.8%, 69.5%, and 69.1%, respectively. It was shown that h^+, $SO_4^{\bullet-}$, and e^- played key roles in the degradation process. After the addition of Furfuryl alcohol (FFA), the degradation rate decreased to 19.0%. The mutual transformation of Co ions and TiO_2 promoted the formation of $SO_4^{\bullet-}$ and e^-/h^+, respectively [19]. $SO_4^{\bullet-}$ was the main ROS in the degradation process (Table S2 in Supporting information). To further verify the presence of active substances in the system, DMPO and TEMP were used as capture agents for EPR analyses. Figs. S5c and d (Supporting information) showed weak DMPO-$^{\bullet}OH$ and DMPO-$SO_4^{\bullet-}$ signals in the PMS system [18], whereas the signal intensities significantly increased in the Co@CNFs-TiO_2-activated PMS system. Co@CNFs-TiO_2 effectively promoted the formation of $SO_4^{\bullet-}$ and $^{\bullet}OH$, which suggests the successful adjustment of the Co valence. The 1:1:1 TEMP-$^1O_2$ signal was also detected and exhibited greater strength in catalytic systems, confirming the contribution of the catalyst.

To clarify the valence changes of Co, high-resolution XPS spectra of Co 2p before and after the reaction were compared and analyzed (Fig. S6 and Table S3 in Supporting information). The Co $2p_{3/2}$ peak shifted from 780.4 eV to 780.8 eV and the Co $2p_{1/2}$ peak shifted from 795.8 eV to 796.4 eV, indicating that the chemical valence state of Co changed. A comparison of the peak areas of the different valence Co fitting peaks before and after the reaction further confirms this result. Before the reaction, the proportions of the split-fitting peak areas of Co(II) and Co(III) were 55.43% (octahedral sites: 22.50%, tetrahedral sites: 32.93%) and 44.57%, respectively. After the reaction in light, the proportion of the split-fitting peak area of Co(II) significantly increased to 62.36% (octahedral sites: 43.86%, tetrahedral sites: 18.50%). Monometallic Co catalysts usually showed a trend of transition from Co(II) to Co(III), that is, the proportion of Co(II) would be reduced. As a result of that, the proportion of Co(II) decreased to 51.09% after the reaction in the dark. The results showed that a cycle occurred between Co(II) and Co(III) in Co@CNFs-TiO_2, resulting in the continuous production of active free radicals [20,21].

Density functional theory (DFT) calculations further elucidated the construction of the catalysts. Optimized structural models of CNFs, Co@CNFs, and Co@CNFs-TiO_2 were displayed in Figs. 4a–c. The distribution of the electrostatic potential (ESP) on the van der Waals surface was used to predict the reaction sites. Fig. 4a showed a CNFs network in which the negative potential was uniformly distributed over the C atom. However, positive potentials appeared when Co and TiO_2 were loaded (Figs. 4b and c). The working functions were further estimated to be 4.202, 3.998, and 3.978 eV (Figs. 4d–f), respectively, confirming the presence of a built-in electric field [21,22]. The facilitation of electron transport by N-doping was also confirmed in the same way (Fig. S7 in Supporting information). Furthermore, the calculated differential charge density image showed that the electron accumulation region appears on the surface of Co, whereas the electron depletion region occurs on the C side (Fig. 4g), which was in accordance with the binding-energy shifts observed in the XPS spectra [23].

Galvanic oxidation system (GOS) was used to determine the electron transfer between light/TiO_2 and varied Co/PMS because electrons could transfer from TiO_2 to Co along the electron channel if the electron-transfer process occurs in catalytic systems (Fig. 4h). PMS/TC and Na_2SO_4 were added to two independent cells connected by an agar salt bridge and an ampere meter. The graphite electrodes in the cells were loaded with Co@CNFs and TiO_2. No significant current generation was observed in the dark environment after the system stabilized, indicating that electron transfer

did not occur. In contrast, in the light environment, GOS coating with TiO_2 showed a high instantaneous current of 12 μA. These results confirmed that light/TiO_2 could trigger electron transfer to Co (Fig. 4i). Furthermore, more TC was oxidized in GOS under light irradiation, indicating that the electron-transfer process could lead to the efficient activation of PMS by Co@CNFs-TiO_2 for TC degradation (Fig. S8 in Supporting information). These results suggested that electrons tend to transfer from TiO_2 to Co through the carbon support. Therefore, it could be speculated that photogenerated electrons and holes generated by TiO_2 promote the mutual conversion to Co(II), thereby improving the ability of Co@CNFs-TiO_2 to activate PMS.

Based on the discussion above, the main catalytic degradation substrates in the Co@CNFs-TiO_2 reaction system include free radical and non-free radical pathways (Fig. S9 in Supporting information). The Co(III)/Co(II) cycle played an important role in free radical pathways. In general, the Co(II) site exposed on the surface of Co_3O_4 could effectively activate PMS by attacking the O–O bond of PMS to produce $SO_4^{\bullet-}$. The presence of an internal electric field from TiO_2 to Co_3O_4 and the conductivity of CNFs could promote electron transfer and accelerate the regeneration of Co(II) [24], thus realizing the continuous generation of $SO_4^{\bullet-}$ and other free radicals. Simultaneously, generated sulfate radicals reacted with HSO_5^- to produce $^1O_2$. In addition, for the non-free radical pathway, singlet oxygen could also be generated by $SO_5^{\bullet-}$ [25]. The TC in the reaction system was eventually oxidized by $SO_4^{\bullet-}$ and other ROS.

In this study, a Co@CNFs-TiO_2 catalyst was successfully synthesized by electrospinning, carbonization, and the sol-gel method. Complete TC degradation was achieved in Co@CNFs-TiO_2 activated PMS system in 15 min with an excellent repetitive capacity. The main reactive species were identified to be $SO_4^{\bullet-}$. Further analyses proved that the electrons generated in the TiO_2 photocatalysis process were transferred to Co, thus reducing the valence state of Co and realizing catalyst regeneration *in situ*. Co(II) continuously and efficiently activates PMS to produce $SO_4^{\bullet-}$ to achieve efficient degradation. N-doping and Co-doping accelerated the electron transport. In this study, efficient catalytic materials were synthesized and guidance was provided for the *in situ* regeneration of transition metal catalysts in PS-AOPs, effectively expanding practical application prospects.

Declaration of competing interest

The authors declare that they have no known competing financial interests or personal relationships that could have appeared to influence the work reported in this paper.

CRediT authorship contribution statement

Ming-Zhen Li: Conceptualization, Writing – original draft. **Yang Zhang:** Conceptualization, Funding acquisition, Methodology, Writing – review & editing. **Kun Li:** Software. **Ya-Nan Shang:** Formal analysis, Software. **Yi-Zhen Zhang:** Data curation, Writing – review & editing. **Yu-Jiao Kan:** Methodology. **Zhi-Yang Jiao:** Data curation, Formal analysis. **Yu-Yuan Han:** Data curation. **Xiao-Qiang Cao:** Funding acquisition, Writing – review & editing.

Acknowledgments

We thank the financial support from the National Natural Science Foundation of China (Nos. 52074176, 52300165, 52300056, 52300099), Natural Science Foundation of Shandong Province Youth Project (No. ZR2022QB155), Open Project Program of Engineering Research Center of Groundwater Pollution Control and Remediation, Ministry of Education of China (No. GW202203).

Supplementary materials

Supplementary material associated with this article can be found, in the online version, at doi:10.1016/j.cclet.2024.109885.

References

[1] T. Man, F. Zhu, Y. Huang, et al., Chin. Chem. Lett. 35 (2024) 109036.
[2] Q. Yang, Y. Ma, F. Chen, et al., Chem. Eng. J. 378 (2019) 122149.
[3] J. Peng, Y. Jiang, S. Wu, et al., Chin. Chem. Lett. 35 (2024) 108903.
[4] J. Li, L. Yang, B. Lai, et al., Chem. Eng. J. 414 (2021) 128674.
[5] J. Li, G. Gou, H. Zhao, et al., Chem. Eng. J. 435 (2022) 134840.
[6] H. Zhao, Y. Ren, C. Liu, et al., J. Hazard. Mater. 459 (2023) 132117.
[7] J. Guo, Y. Wang, Y. Shang, et al., Proc. Natl. Acad. Sci. U. S. A. 121 (2024) e2313387121.
[8] K. Yin, Y. Shang, D. Chen, et al., Appl. Catal. B: Environ. 338 (2023) 123029.
[9] B.T. Zhang, Y. Zhang, Y.G. Teng, Appl. Surf. Sci. 452 (2018) 443–450.
[10] D. Wang, M. Suo, S. Lai, et al., Appl. Catal. B: Environ. 321 (2023) 122054.
[11] Y. Shang, Y. Kan, X. Xu, Chin. Chem. Lett. 34 (2023) 108278.
[12] M. Zhang, J. He, Y. Chen, et al., Chin. Chem. Lett. 31 (2020) 2721–2724.
[13] W. Wang, G. Zhang, Q. Wang, et al., Chin. Chem. Lett. 35 (2024) 109193.
[14] S.Y. Shen, T. Ke, D.K. Fang, et al., J. Hazard. Mater. 297 (2022) 121460.
[15] A.Q. Wang, Z. Chen, Z.K. Zheng, et al., Chem. Eng. J. 379 (2020) 122340.
[16] K. Yin, R. Wu, Y. Shang, et al., Appl. Catal. B: Environ. 329 (2023) 122558.
[17] Q. Yang, Y.H. Ma, F. Chen, et al., Chem. Eng. J. 378 (2019) 122149.
[18] Y. Zhang, B.T. Zhang, Y.G. Teng, et al., J. Hazard. Mater. 400 (2020) 123290.
[19] J.L. Jia, D.M. Liu, S.X. Wang, et al., Sep. Purif. Technol. 253 (2020) 117510.
[20] Y. Fan, Y.F. Ji, G.Y. Zheng, et al., Chem. Eng. J. 330 (2017) 831–839.
[21] M.H. Xiong, J.T. Yan, G.Z. Fan, et al., Chem. Eng. J. 444 (2022) 136589.
[22] C. Liang, H.P. Feng, H.Y. Niu, et al., Chem. Eng. J. 384 (2020) 123236.
[23] H. Xu, J.R. Li, X.X. Chu, Nanoscale Horiz. 8 (2023) 441–452.
[24] W. Ren, L.L. Xiong, X.H. Yuan, et al., J. Hazard. Mater. 53 (2019) 14595–14603.
[25] J.A. Jing, X.C. Wang, M.H. Zhou, Water Res. 232 (2023) 119682.